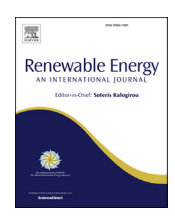


Contents lists available at ScienceDirect

Renewable Energy

journal homepage: www.elsevier.com/locate/renene



Towards a better understanding of yawed turbine wake for efficient wake steering in tidal arrays



Pranav K. Modali, Ashwin Vinod, Arindam Banerjee

Mechanical Engineering & Mechanics, Lehigh University, Bethlehem, PA, USA

ARTICLE INFO

Article history: Received 14 July 2020 Received in revised form 25 May 2021 Accepted 26 May 2021 Available online 1 June 2021

Keywords: Tidal turbine yaw Near-wake turbulence Energy recovery Wake-steering

ABSTRACT

Tidal stream turbines (TST) deployed in open-water energetic sites are often unintentionally at yaw to the incoming flow that causes performance degradation and deflection of the wake. Wake steering is a popular concept in wind arrays where the upstream turbine is operated intentionally at yaw to steer the wake away from a downstream turbine. To explore such arrangements for TST arrays, a synergistic experimental and numerical campaign was undertaken to characterize a TST performance and wake deflection subjected to $\pm 15^{\circ}$ yawed inflow. The near-wake characterization study was performed using complementary acoustic Doppler velocimetry measurements and 3D computational fluid dynamics. The experiments show a ~10% reduction in the maximum power coefficient. In the near field, the deflected wake morphed into an elliptical shape due to the formation of two counter-rotating vortices. The wake deflection results in enhanced momentum transfer and dissipation, leading to accelerated energy recovery. When the upstream turbine is yawed, available kinetic energy in the flow for the downstream turbine is at least 50% higher with the turbine array in a staggered configuration compared to the inline configuration. Our results provide guidance in reducing the cross-stream and downstream spacing between turbine units in an array.

© 2021 Elsevier Ltd. All rights reserved.

1. Introduction

Tidal Stream Turbines (TST) are renewable energy devices used to harness power from tides, rivers, and streams without requiring any obstruction to the natural flow of water [1]. Studies in scientific literature related to TST hydrodynamics can be broadly classified into two categories. The first category focuses on the energy extracted by TST from the flow and mostly deals with methods for improving the device performance [2-13]. The focus of the second category is on the wake region behind TST and the development of models to characterize the momentum deficit as well as the high level of turbulence in the wake [14–20]. A thorough understanding of wake propagation is essential in developing optimized tidal turbine array layouts. Turbine wake development, propagation, and recovery are influenced by turbine operating conditions as well as external factors such as ambient turbulence [16,21-23], sheared inflow [24,25], and yaw misalignment [26-29]. A thorough understanding of the influence of these external factors on turbine

performance, wake development, and its interaction with downstream turbine units is vital to developing efficient and robust tidal turbine array layouts. One popular concept with wind array operators to minimize interaction between turbines within the array and increase the annual energy production is wake-steering. The upstream turbines in an array are operated at yaw such that the wake is steered away from the downstream turbine allowing for a closely packed array [30,31]. Such practices are gaining popularity in wind-array operations and can be extended to tidal flows where the available area for array deployment is limited due to restrictions placed for navigational, environmental, and recreational restrictions.

A yawed inflow may occur naturally due to wave-current interaction [29], directional changes in ebb and flood tides [32], and the presence of upstream bluff bodies or turbine support structures [32,33]. Computational fluid dynamics (CFD) studies [34,35] have been conducted to explore the influence of yaw on turbine performance; a ~4% power reduction was reported as the inflow angle changes from zero to 10° yaw [35], and in a different study ~7.4% power reduction was reported for a change in inflow angle to 15° yaw [34]. Early computational work also focused on the fluid-structure interaction problem to understand turbine performance

^{*} Corresponding author. E-mail address: arb612@lehigh.edu (A. Banerjee).

Renewable Energy 177 (2021) 482-494

Nomenclature C_T Thrust coefficient			
		Cd_{ω}	Cross-diffusion term in RANS model
		D	Diameter
Acronyms		D_{ω}	Dissipation term
ADV	Acoustic Doppler velocimetry	E	Flow energy available
CFD	Computational fluid dynamics	F	Frequency
CVP	Counter-rotating vortex pair	F_B	Blade passing frequency
RANS	Reynolds averaged Navier-Stokes	F_R	Turbine rotor frequency
RMS	Root mean square	f_R	Reaction thrust
RPM	Rotations per minute	f_{r1}	Curvature correction term
SST	Shear stress transport	f_{x}	Stream-wise force component
TKE	Turbulent kinetic energy	f_Z	Cross-stream force component
TSR	Tip speed ratio	g	Acceleration due to gravity
TST	Tidal stream turbine	k	Turbulent kinetic energy
		N	Total number of samples
Greek Symbols		n	Cosine-fit index
α	Volume fraction	p	Pressure
γ	Yaw angle	Re	Reynolds number (diameter based)
ε	Turbulence dissipation rate	S_{ij}	Strain rate tensor
μ	Fluid dynamic viscosity	T	Thrust
μ_t	Eddy viscosity	t	Total time
ν	Kinematic viscosity	Ti	Turbulence intensity (%)
ρ	Density	U	Time averaged streamwise velocity
σ	Standard deviation	U*	Non-dimensional streamwise velocity
au	Torque	U_r	Relative velocity in rotating reference frame
$ au_f$	Viscous stress tensor	u'	Reynolds-averaged fluctuating velocity
ω	Turbulent eddy frequency	U_{∞}	Freestream velocity
Ω ij	Rotation tensor	V*	Non-dimensional cross-stream velocity (vertical)
		W*	Non-dimensional cross-stream velocity (horizontal)
Symbols		X	Downstream direction
Α	Area of the turbine rotor	y	Vertical direction
В	Area-based blockage ratio (%)	y^+	Dimensionless wall distance
С	Chord length of the rotor	Z	Cross-stream direction
C_P	Power coefficient		

deterioration due to yawed inflow [35]. More dramatic changes in a flow direction that resulted in a complete reversal in the flow direction as in a tidal channel were studied computationally by Frost et al. [32]. The reversal in tides resulted in the support structure (stanchion or pylon) being present upstream or downstream of the turbine. A drop in power performance was observed when the turbine was placed in the shadow of the support structure; a yaw mechanism was recommended for performance enhancement [32]. The wake behavior for a yawed inflow case is very different from the no-yaw case [27,28,36-38]. Baratchi et al. [37] used an actuator line method coupled with a large eddy simulation approach to observe accelerated wake dissipation for the yawed case at hub height. Frost et al. [28] extended their CFD study using field data from Ramsey Sound (Wales, U.K.) to initialize their numerical simulations. At this location, the flow was observed to yaw around $\pm 20^{\circ}$ to the turbine rotor; the authors reported an accelerated wake recovery of ~90% by 7D downstream for a yawed inflow of ±10° compared to 10D downstream distance for the no-yaw case [28]. Controlled laboratory experiments were performed by Maganga et al. [38] to quantify the effects of yaw on the performance, wake, and loading of the turbine; a turbine yaw resulted in a drop in performance. Galloway et al. [29,36] used a combination of laboratory experiments and blade element momentum analysis to study cyclic loading and fatigue effects due to dynamic yaw on the rotor caused by a wavecurrent interaction; a yaw below 7.5° had negligible effect on the rotor. To summarize, majority of the earlier studies reported performance degradation of a turbine subjected to yawed inflow with

only one-study [28] focusing on downstream wake propagation and recovery in the far-field (>10D downstream).

In the current study, we use complementary laboratory experiments and blade-resolved CFD simulations to study turbine performance and wake propagation in the near field ($\leq 5D$) for yaw angles (γ) of $\pm 15^{\circ}$; the results are then compared to a baseline case of no-yaw. To the authors' knowledge, the near-wake turbulence measurements using acoustic Doppler velocimetry (ADV) are the first such measurements of near-wake statistics of a tidal turbine under vawed inflow. The three-dimensional transient CFD simulations complement the experiments and provide a detailed characterization of wake asymmetry and downstream energy recovery. These estimates are then used to study wake interaction between two turbines in an array. The concept of wake-steering [31] is then utilized to explore the effects of the upstream turbine yaw on the energy recovery and downstream spacing between two turbines in an array. Data presented in this study is expected to provide an insight for wake predictions of yawed tidal turbines in open-water deployment and array designs.

2. Methods

Fig. 1a shows the free-body diagram for the yawed inflow, where γ is the yaw angle. Non-dimensional parameters used to characterize the performance of the turbine include the tip speed ratio (*TSR*), the power coefficient (C_p), and the thrust coefficient (C_T) defined below:

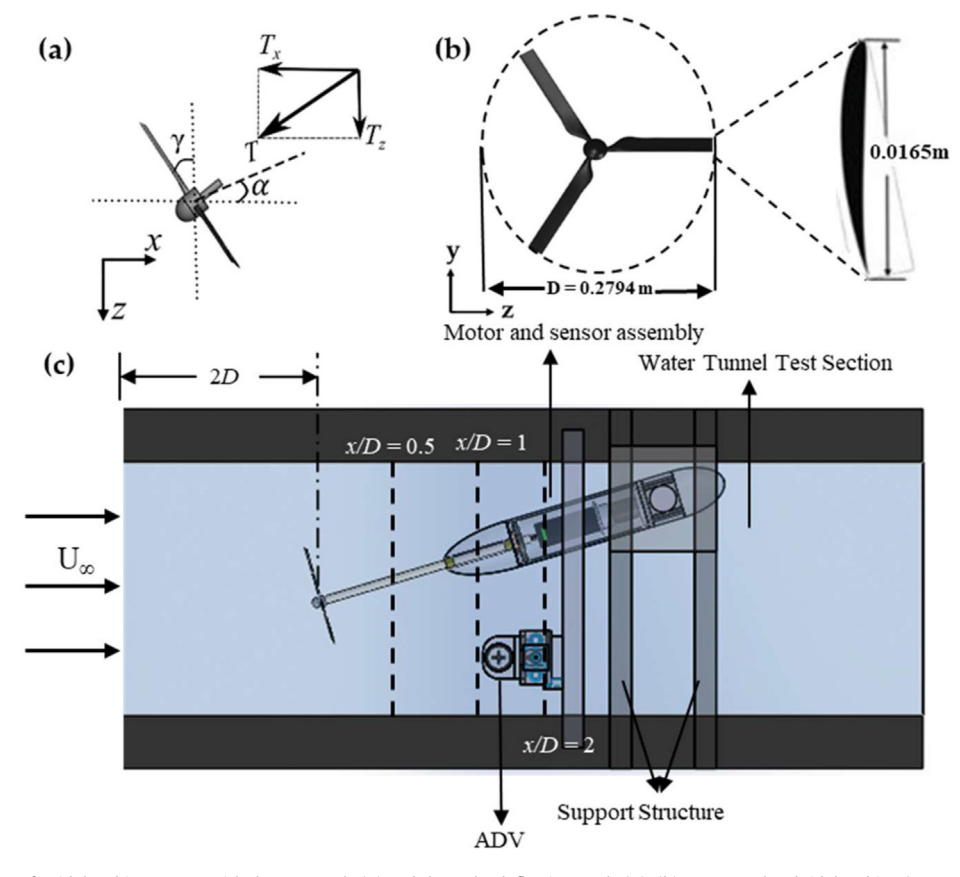


Fig. 1. (a) Free body diagram of a tidal turbine at yaw with the yaw angle (γ) and the wake deflection angle (α) ; (b) constant chord tidal turbine (1:20 model, D=0.2794 m) used in the current study with SG6043 blade cross-section; (c) Experimental setup for validation and verification of CFD depicting velocity measurements conducted using an acoustic Doppler velocimeter (ADV) at locations x/D=0.5 to 2 (donated by dashed lines) behind the turbine.

$$TSR = \frac{QD}{2U_{\infty}}, \ C_P = \frac{P_{out}}{1/2 \ \rho AU_{\infty}^3}, \ C_T = \frac{T}{1/2 \ \rho AU_{\infty}^2}$$
 (1)

where D is the diameter of the turbine (m), Ω is the rotor rotational speed (rad/s), U_{∞} is the freestream velocity (m/s), $P_{\text{out}} (= \tau \times \Omega)$ is the turbine power output (Watts), ρ is the density of the fluid (water) (kg/m^3) , τ is the torque on the turbine $(N \cdot m)$, T is the thrust force on the turbine (N), and A was the rotor swept area (m^2) . Measured thrust and torque values were blockage corrected using the technique suggested by Bahaj et al. [39].

2.1. Experimental setup

All experiments reported in this paper were conducted using a three-bladed horizontal axis TST (1:20 scale) with a diameter of 0.2794 m (see Fig. 1b). The turbine blades were made of a constant chord, untwisted SG-6043 hydrofoil profile, chosen to maximize the lift coefficient in the operational Reynolds number range of 10^5-10^6 and used in previous studies by our group [5,15,16,40]. The experiments were conducted at Lehigh University (PA, USA) in an open surface water tunnel with a cross-sectional area of $0.61~\text{m}\times0.61~\text{m}$ with a test section that was 1.98~m long. The tunnel cross-section resulted in an area blockage ratio (B) of 16.5% for the no-yaw case and a slightly reduced 15.4% blockage for the $\pm15^\circ$ yaw cases. The experimental setup (shown in Fig. 1c) primarily consists of the turbine blades attached in line to a stepper motor and a thrust-toque sensor assembly, both of which are enclosed in a dry acrylic casing. The stepper motor (Anaheim Automation, Model#

23MSDI) is used to precisely control rotor rotational speeds with a resolution of 1600 steps/rotation. The thrust-torque sensor assembly is used to measure the thrust (T) and the torque (τ) acting on the rotating turbine blades at the rate of 200 samples/second. A Nortek Vectrino + ADV was used to measure velocities in the flow field. Wake measurements were made at hub height at three downstream locations, 0.5D, 1D, and 2D, from the rotor plane. At each downstream location, measurements were made at a total of 41 (equally spaced) points across the cross-stream direction with a spacing of 0.05D between each point. In the current study, z denotes the cross-stream direction and y denotes the vertical direction; consequently, v and w velocity components measured by ADV denote vertical and cross-stream direction, respectively. The ADV time traces were filtered using the phase space thresholding technique to eliminate spikes and ensure quality data for further analysis, as described in Goring and Nikora [16]. With the help of this technique, the spikes and outliers are identified to be replaced with the mean of the time trace. Each velocity component (u(t), v(t), v(t),and w(t)) obtained can be broken down as

$$u(t) = U + u'(t) \tag{3}$$

where U is the time-averaged velocity component and u'(t) is the time-dependent fluctuating component. One-dimensional turbulence intensity (Ti) from the velocity components is defined as

$$Ti = 100 \times \sqrt{u'^2} / U \tag{4}$$

P.K. Modali, A. Vinod and A. Banerjee Renewable Energy 177 (2021) 482–494

A convergence test was first performed to determine the appropriate sampling period for the experiments. U and $\sigma(u)$, which represent the mean and standard deviation ($\sigma(u) = \sqrt{u'^2}$) of the streamwise velocity was sampled for a total of 300 s at each measurement location at a frequency of 50 Hz. Percentage error is evaluated and plotted in Fig. 2 as:

% Error =
$$100*|(X_n-X_m)/X_n|$$
, (5)

 X_n is the parameter value of the complete time trace, and X_m is the same parameter value calculated from inception to the current second, m, ranging from 1 to 300 s. The % Error for both U and $\sigma(u)$ can be observed to drop below 3% at $t \geq 30$ s. A more conservative 120 s sampling period was thus used for all wake measurements. An inlet flow velocity (U_∞) of 0.73 m/s was selected as it was determined that turbine performance was only weakly sensitive to Reynolds number effects beyond that value based on an earlier Reynolds number dependency study conducted on the same turbine model [15].

2.2. Computational setup & governing equations

Reynolds Averaged Navier-Stokes (RANS) equations coupled with a k- ω shear stress transport (SST) turbulence model with curvature correction were solved. The conservation of mass and momentum equations can be written as:

$$\nabla \cdot \overrightarrow{U}_r = 0 \tag{6}$$

$$\left[\frac{\partial}{\partial t} \left(\rho \overrightarrow{U}\right) + \nabla \cdot \left(\rho \overrightarrow{U}_r \otimes \overrightarrow{U}_r\right) + \rho \left(\overrightarrow{\Omega} \times \overrightarrow{U}_r + \overrightarrow{\Omega} \times \overrightarrow{\Omega} \times \overrightarrow{r}\right)\right] \\
= -\nabla p + \nabla \cdot \tau_f$$
(7)

where the relative velocity $\overrightarrow{U}_r(=\overrightarrow{U}-\overrightarrow{\mathcal{Q}}\times\overrightarrow{r})$ is viewed from a rotating reference frame, $\rho(\overrightarrow{\mathcal{Q}}\times\overrightarrow{U}_r)$ $\rho(\overrightarrow{\mathcal{Q}}\times\overrightarrow{U}_r)$ and $\rho(\overrightarrow{\mathcal{Q}}\times\overrightarrow{\mathcal{Q}}\times\overrightarrow{r})$ are the Coriolis force and the centrifugal force, respectively, p is the pressure and τ_f is the viscous stress tensor. The κ - ω SST model was chosen for its efficiency in predicting fluid flows under adverse pressure gradients [41]. The production term in κ and ω equations was modified with a curvature correction term f_{r1} as:

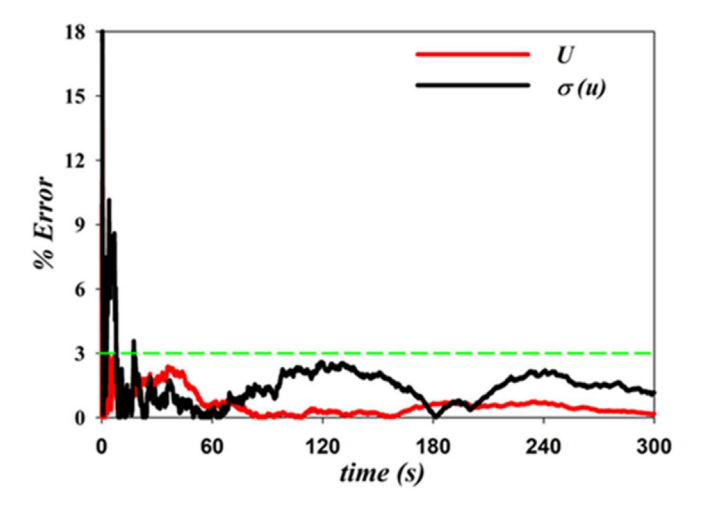


Fig. 2. Effect of sampling period on time-averaged velocity U, its standard deviation $\sigma(u)$.

$$\frac{\partial(\rho k)}{\partial t} + \frac{\partial(\rho u_i k)}{\partial x_i} = P_k f_{r1} - \beta k \omega + \frac{\partial}{\partial x_i} \left[(\mu + \sigma_k \mu_t) \frac{\partial k}{\partial x_i} \right]$$
(8a)

$$\frac{\partial(\rho\omega)}{\partial t} + \frac{\partial(\rho u_j\omega)}{\partial x_j} = \alpha \rho \frac{P_k}{\mu_t} f_{r1} - D_\omega + C d_\omega + \frac{\partial}{\partial x_j} \left[(\mu + \sigma_\omega \mu_t) \frac{\partial \omega}{\partial x_j} \right]$$
(8b)

where $\alpha=\alpha_1 F + \alpha_2 (1-F)$, $\alpha_1=5/9$, $\alpha_2=0.44$, $\beta^*=0.09$, are empirical constants of the SST model, μ and μ_t are molecular and eddy viscosity respectively, Cd_ω is the cross-diffusion term in the SST model, D_ω is the dissipation term in Eq. (8b) [42]. The modified curvature function is defined as:

$$f_{r1} = \max\{ \min(f_{rotation}, 1.25), 0 \},$$

$$f_{rotation} = (1 + c_{r1}) \frac{2r^*}{1 + r^*} \left[1 - c_{r3} \tan^{-1}(c_{r2}\tilde{r}) \right] - c_{r1}$$
(9)

where $c_{r1}(=1)$, $c_{r2}(=2)$ and $c_{r3}(=1)$ were constants [41,43]; \tilde{r} and r^* were given as:

$$\tilde{r} = 2\Omega_{ij}S_{jk} \left[\frac{D_cS_{ij}}{D_ct} + \left(\varepsilon_{imn}S_{jn} + \varepsilon_{jmn}S_{in} \right) \Omega_m^{rot} \right] \frac{1}{\Omega D_c^3},
r^* = \frac{S}{O}, \qquad S^2 = 2S_{ij}S_{ij} \quad and \quad \Omega^2 = 2\Omega_{ij}\Omega_{ij}.$$
(10)

 S_{ij} was the strain rate tensor, Ω_{ij} was the rotation tensor, ω was the turbulent eddy frequency, ε_{ijk} is the Levi-Civita operator, and variable D_C was defined as:

$$D_c^2 = \max(S^2, 0.09\omega^2) \tag{11}$$

Simulations were set up to provide a more detailed description of the flow field to supplement our experimental measurements and quantify the wake characteristics. The nacelle body and post are not included in the CFD model to allow for an undisturbed wake (see Fig. 3a). While the CFD validation is done with the experiments by mimicking the experimental setup with B = 16.5%, the rest of the simulations are set up to reduce the area-based blockage ratio to <5%. This was done keeping in mind open water deployment conditions which are more unrestrictive and beyond the scale of the current experimental facility (B = 16.5%) or almost any laboratory facility. Recent experiments by Ross and Polagye [44] with a cross-flow turbine have demonstrated that decreasing the width of the experimental channel while holding the water depth constant decreased the extent of the wake in the lateral direction. We thus chose to discuss the implications of blockage to turbine wake parameters under yaw by complementing our experimental measurements with three-dimensional transient CFD simulations at a blockage ratio of <5%; the lower blockage was obtained by doubling the cross-sectional area of our experimental flume to $1.22 \text{ m} \times 1.22 \text{ m}.$

The computational domain consists of two sub-domains, a rotating inner domain and a stationary outer domain (see Fig. 3a and b). The turbine is located in the inner domain that is located 3.25D from the inlet and 5D from the outlet; the size of this rotating sub-domain is $1.1D \times 0.275D$. The interfaces between the rotating and stationary domains were kept to a minimum by shaping the inner rotating domain as a cylinder (as shown in Fig. 3b), thereby limiting the interfaces to three (front face, back face, and circumferential face) to eliminate any numerical artifacts in the downstream wake. Interface boundary is the face shared between the stationary outer domain (using stationary solver) and the rotating inner domain (using rotating solver). The domain outlet was

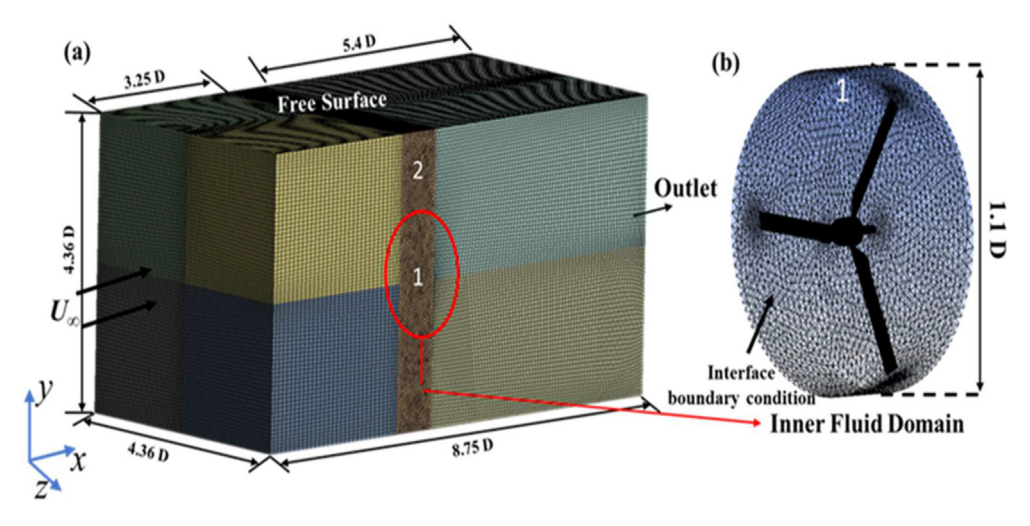


Fig. 3. (a) Structured computational mesh and unstructured computational mesh (1 and 2) used for the study; (b) rotating inner fluid domain (1).

specified as an outlet boundary condition with an average relative pressure of zero. The walls of the domain (side and bottom) and the turbine are specified with the no-slip wall condition, while the domain top was modeled as zero relative opening pressure to simulate free-surface. A buoyancy model was activated for the rotating inner domain. The simulation was set to converge after the scaled residuals of continuity, momentum, and turbulence quantities fell below 1×10^{-4} at each time step. Time step size corresponding to 2° rotation was chosen and was found to be numerically stable based on an earlier analysis by our group [15]. Details of flow and turbine parameters used for CFD are listed in Table 1. The computational mesh contains structured (unnumbered segments in Fig. 3a) and unstructured mesh (segments 1, 2 in Fig. 3a and b) elements. A moving mesh technique was employed where the inner fluid domain (see Fig. 3b), containing the turbine model, would rotate at a set rotational speed during each time-step until convergence of momentum and continuity equations was reached. In addition to a torque-based mesh convergence study [27] by varying mesh size from 8 to 19 million elements, a velocity-based mesh convergence study was also conducted with the primary goal of obtaining convergence in the wake profiles; based on the obtained results, a domain containing 11 million mesh elements was selected as it restricted the maximum error (for both velocity and torque) to < 1%. The mesh quality was maintained by containing the y^+ values within the range $3 < y^+ <$ 10 to appropriately capture the boundary layer separation at the rotor blades. In the current simulations, the wake shape and wake path become invariant with time after a total of 16 turbine rotations that corresponds to ~ 4 s of real-time in the CFD simulations. To ensure that the contour plots do not have any transient features, we

Table 1 Flow and turbine parameters for CFD analysis.

Simulation Parameters	Value
Blade profile	SG-6043
Density of water (ρ)	998.2 kg/m ³
Temperature of water	25 °C
Pressure (p)	101.3 kPa
TST rotor diameter (D)	0.2794 m
Chord length (c)	0.0165 m
Number of blades	3
Rotor speed (rpm)	250
Freestream velocity (U_{∞})	0.73 m/s
Reynolds number (diameter based)	2.04×10^{5}

plot normalized velocity contours at t=5 s. The data sets discussed correspond to TSR where peak turbine performance was observed with the blades rotating in a clockwise direction similar to experimental setup.

Tracking the wake trajectory is important for open-water deployment and for determining the position of a downstream turbine in a tidal array. The wake trajectory is tracked by estimating the center of wake; various methods are available in the literature to measure the wake center, and these methods are dependent on the fidelity of the available datasets, i.e., one-dimensional (profile/line) and two-dimensional (planar) data sets. In the current study, the authors have used the Center of Mass (CoM) technique in which the wake is considered as a solid body, and the center is estimated as the weighted average of the wake velocity deficit [45]. Typically, this can be done taking a line measurement of velocity data at the hub height (y = 0), and is defined as,

$$z_{C,1D}(x) = \int z \Delta U(x,z) dz / \int \Delta U(x,z) dz$$
 (12a)

where $z_{C,1D}$, is considered the 1D center of wake and ΔU (= $U_{\infty} - u(x,y,z)$) is the velocity deficit, and u(x,y,z) is the instantaneous velocity. To consider the vertical meandering of the wake, the definition can be expanded to the 2D center of wake coordinates as:

$$y_{c,2D}(x) = \iint y \Delta U(x,y,z) dy dz / \iint \Delta U(x,y,z) dy dz$$

$$z_{c,2D}(x) = \iint z \Delta U(x,y,z) dy dz / \iint \Delta U(x,y,z) dy dz$$
(12b)

For the CoM technique, the wake bounds are assumed to be 99% of the free-stream velocity [27]. This technique considers the change in shape and is sensitive to the large velocity gradients near the wake bounds.

2.3. Validation and verification

The computations were first validated by comparing the C_P and C_T estimated from CFD with the experiments; both data sets were blockage corrected using the technique suggested by Bahaj et al. [39]. With increasing yaw angle, the magnitude of both C_P and C_T was observed to decrease, as seen in Fig. 4a and b. The experimental performance data over-predicts the transient simulations by \sim 6–8% for no yaw and positive yaw cases. Experimental blockage

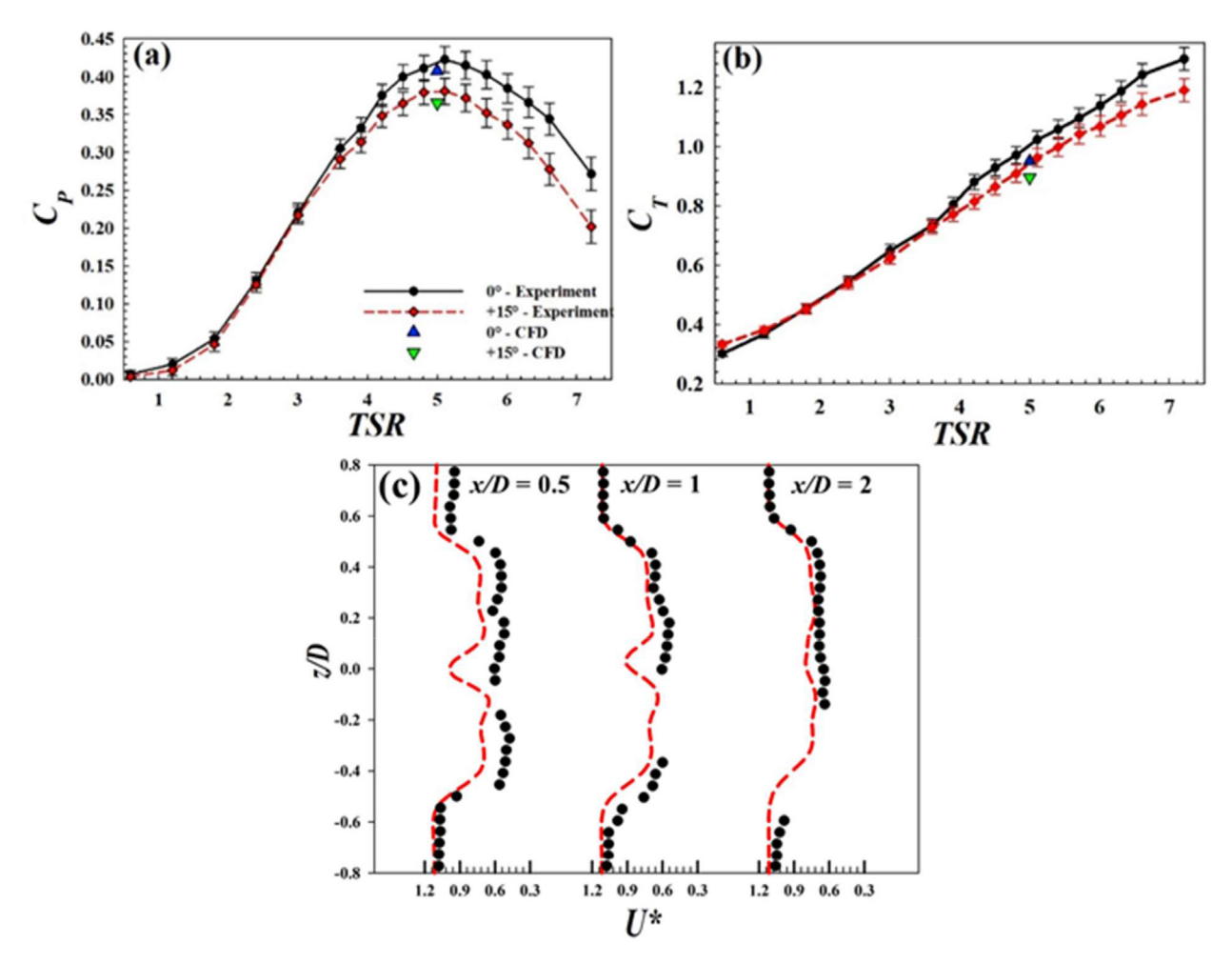


Fig. 4. (a) Power coefficient ($C_{\rm P}$), and, (b) Thrust coefficient ($C_{\rm T}$) comparison for $\gamma=0^{\circ}$ and $\gamma=15^{\circ}$ yaw cases between CFD transient simulations and experimental data (both with blockage correction); (c) Comparison of hub-height velocity profiles behind a turbine ($\gamma=-15^{\circ}$ yaw, TSR=4.8) at three different downstream locations at B=16.5% (the black dots (\bullet) are the experimental ADV measurements while the red dotted line (-) is data from CFD runs). Both sets of experimental and CFD results are at B=16.5%.

corrected TSR, where peak performance was observed, is slightly higher compared to simulations. To broaden the validation envelop, velocity profiles in the turbine wake obtained from CFD were validated by comparing them to experimental flow measurements for the 15° yaw case. The CFD domain is set up to mimic the experimental domain with the same blockage (16.5%) for validation simulations. A normalized velocity $U^* = U/U_{\infty}$, where U is the timeaveraged (local) velocity, is compared at three downstream locations of x/D = 0.5, 1, and 2, with the turbine experiencing $+15^{\circ}$ yawed inflow. As shown in Fig. 4c, both the data sets are in good agreement regarding the wake shape and wake width. The velocity profile at these near-wake locations was observed to have a top-hat profile, as reported in models of similar flows [14]. At locations closer to the turbine rotor, the experimental study experienced a higher deficit (~ 18%) than the simulations due to the presence of the nacelle. With increasing downstream distance (x/D = 2), the deficit for experimental and simulation data can be observed to be comparable.

3. Results

3.1. Effect of yaw on turbine performance

The effect of yaw on the performance of a TST was analyzed by comparing C_P measured at 15° yaw to the (baseline) case of 0° yaw;

the rotational speed of the turbine was varied over a TSR range of 0.6-6.3 that corresponds to a range of 30-360 rpm. The comparison plot is presented in Fig. 4a. The change in the performance was observed to be negligible between 0° and 15° cases at TSR <3, beyond which the curves diverge with increasing TSR. Peak power performance ($C_{P. max}$) is observed at $TSR \sim 4.8$ (250 rpm) for both the no yaw and 15° yaw cases. A power deficit of ~8.7% was observed for 15° yaw cases at peak performance, while a maximum deficit of ~29% was observed at maximum TSR = 6.3. Similar observations were made for the thrust experienced by the turbine with yawed inflow, as can be seen in Fig. 4b. The change in C_T for all presented angles at TSR < 3 is negligible, beyond which the C_T curves were observed to diverge with increasing TSR with the thrust force decreasing with increasing yaw angle. A thrust reduction of ~9% was observed for 15° yaw angle at peak TSR; a maximum thrust reduction of $\sim 10\%$ was observed at TSR = 6.3.

Fig. 5 compares normalized power reduction at peak performance from the current (blockage corrected) experimental data with previous studies [26,28,35,39,46]. The data is normalized based on the peak performance for the no-yaw case. Our experimental data can be seen to be in close agreement with the observations of Galloway et al. [26] and Park et al. [35]. The performance and thrust reduction were compared to a theoretical estimate based on momentum balance analysis [47]; it correlates the performance drop in yawed cases to the decrease in effective flow

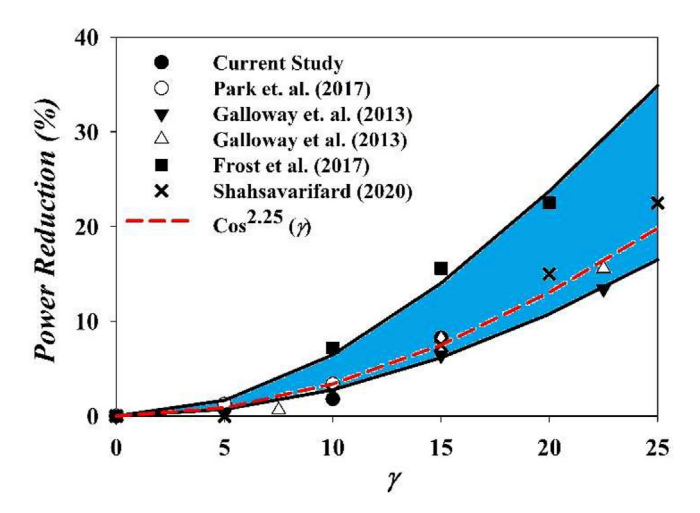


Fig. 5. Power reduction comparison with different previous studies for varying yaw angle and cosine-fit for current (blockage corrected) experimental data at B = 16.5% [26,28,35,39,46].

velocity and projected turbine swept area via the relationship, $\cos^n(\gamma)$, where n is the reduction index for power/thrust. The reduction index for previous studies [26,28,35,39,46] can be observed to vary from 1.83 to 4.36 (shaded region in Fig. 5). The experiments reported here result in a power reduction index of 2.25. A majority of the studies report an index lower than the theoretical value of 3, the only exception being the study by Frost et al. [28], who report a power reduction index value of 4.36.

3.2. Wake turbulence statistics

3.2.1. Velocity profiles and wake meandering

Next, we discuss the results of our wake generated by the turbine. We start with ADV measurements behind the rotor plane at three downstream locations of x/D=0.5, 1, and 2 at hub height. As mentioned earlier, the experimental flume has a cross-section area of 0.6096 m \times 0.6096 m resulting in a blockage ratio of 16%. Similarsized blockage/flumes have been used in other studies [8,48–50]. All the wake measurements correspond to the turbine operating at $C_{p,\ max}$ (i.e., $TSR\approx4.8$). Fig. 6a—c compares the effect of γ on the normalized mean velocity profile ($U^*=U/U_\infty$) along the spanwise direction at the three downstream locations. The velocity distribution for all cases mimics a top-hat profile suggesting an undiffused wake along with ~10% acceleration in the wake bypass region

due to tunnel blockage effects. For the no-yaw case, the velocity profile was observed to be symmetric about the centerline with a deficit recovery of ~17% as the wake reaches x/D=2. The velocity profiles for both $+15^{\circ}$ and -15° yaw are a mirror image of each other and are comparable in terms of the velocity magnitude. At locations close to the turbine (x/D=0.5), the velocity is evenly distributed inside the wake for the yawed cases. A velocity recovery of ~25% was observed at x/D=2, which is ~8% higher than the no-yaw case suggesting a faster recovery at hub height.

The direction of wake deflection can be explained using a freebody diagram of a yawed turbine (see Fig. 1a). In situations where the free-stream velocity (U_{∞}) is at yaw (γ) , a component of velocity $(U_{\infty}\cos\gamma)$ that is normal to the rotor provides a principal thrust (T)on the turbine rotor, which results in a reaction thrust (f_R) by the turbine that was resolved into two mutually perpendicular components; a stream-wise component (f_x) and cross-stream component (f_z) as shown in Fig. 1a. The reaction force component f_z imparted on the flow by the rotor is conjectured to be the driving mechanism behind the direction of wake deflection observed. Fig. 7 presents the contours for normalized streamwise ($U^* = U/U_{\infty}$), depth-wise ($V^* = V/U_{\infty}$), and cross-stream ($W^* = W/U_{\infty}$) velocity components for both -15° and $+15^{\circ}$ yaw cases; the results are compared with the reference no-yaw case. A slowdown of the stream-wise velocity component was observed upstream of the turbine for all three cases. A slowdown was observed further upstream for the yawed cases. From the *U** velocity contour, the wake was observed to be fairly symmetric about the turbine axis for the no-yaw case as the wake propagation is aligned with the freestream flow. However, for $\gamma = \pm 15^{\circ}$ cases, the wake is asymmetric; the wake propagates downstream at an angle to the free stream. The cross-stream tangential thrust force (f_z) primarily determines the downstream wake deflection direction as the yaw angle γ is switched between $\pm 15^{\circ}$ due to yawed inflow. For the $\gamma = +15^{\circ}$ yaw case, both the deflection direction (shown in Fig. 7) and f_z (see Fig. 1a) is in -z direction; the direction is reversed for $\gamma = -15^{\circ}$ yaw. Reduction in-wall effects due to reducing the blockage ratio can be observed by looking at the bypass flow acceleration. Free-stream acceleration in the bypass region is observed to reduce by 50% (from ~10% acceleration in experiments as shown in Fig. 7 to ~5% acceleration). As observed in Fig. 7, the cross-stream and depth-wise velocity components (V^* and W^*) have a larger magnitude for yawed cases due to wake deflection. The V^* velocity contours demonstrate a wake that is rotating in the counter-clockwise direction and is opposite to the clockwise rotation of the TST. A large magnitude of W* velocity component is observed close to the blade tip for all cases. At this location, the

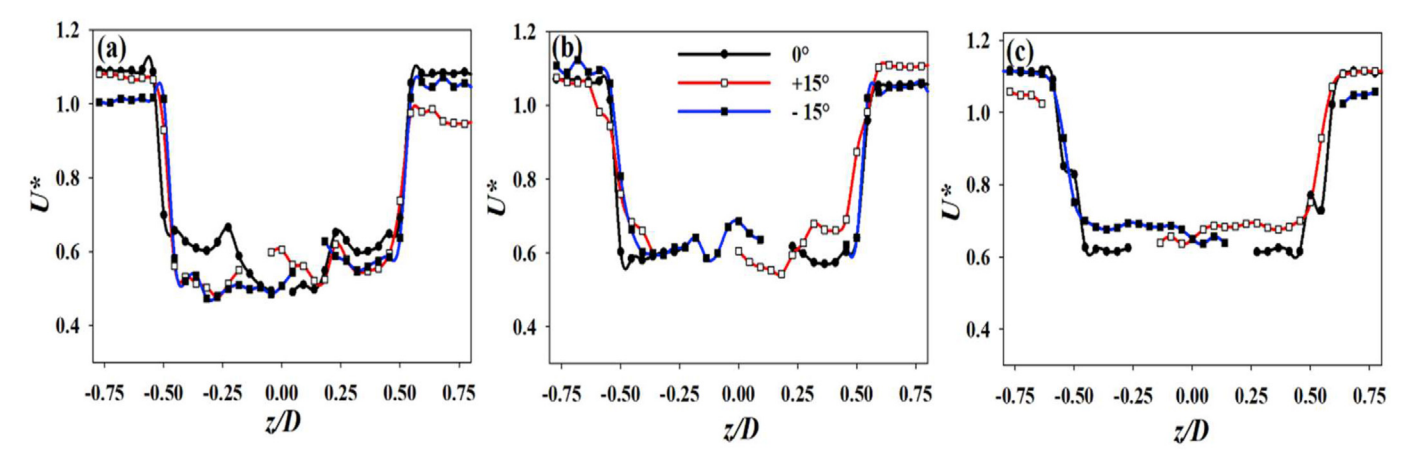


Fig. 6. Normalized velocity profiles U^* for $\gamma=0^\circ$, -15° and $+15^\circ$ at (a) x/D=0.5, (b) x/D=1, and (c) x/D=2 at hub height (y=0) from experimental data at B=-16.5%.

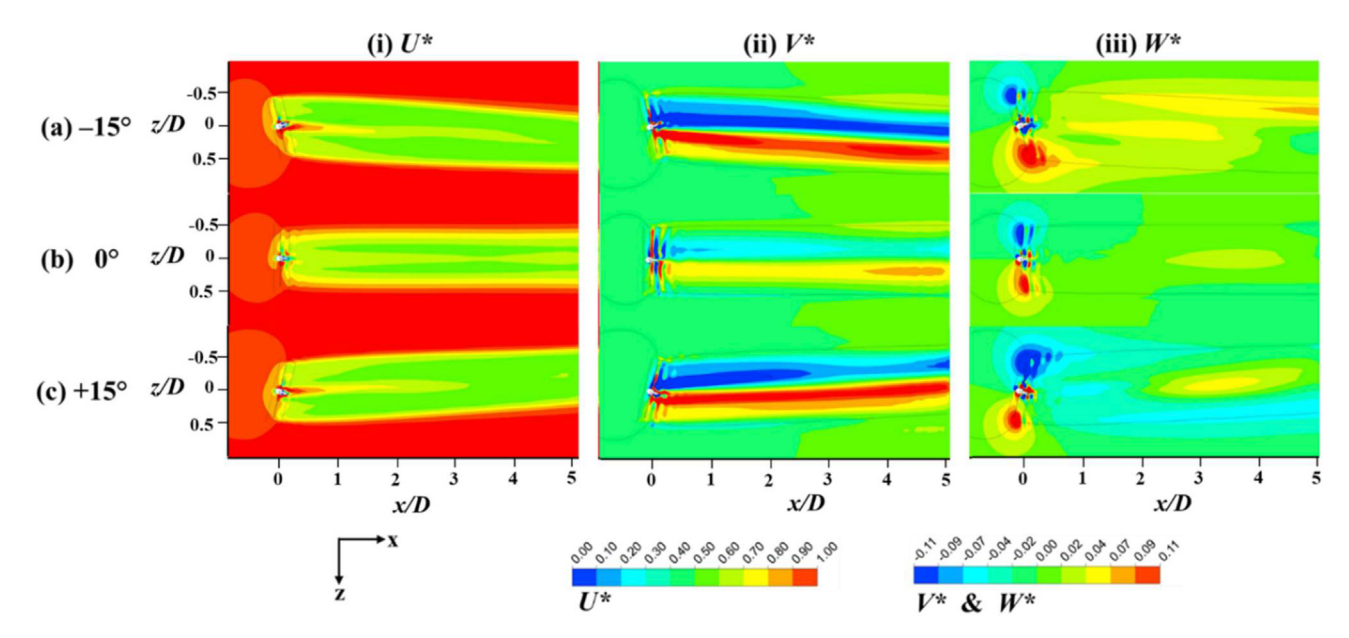


Fig. 7. Normalized velocities U^* , V^* and W^* for $\gamma=0^\circ$, -15° and $+15^\circ$ cases on the XZ plane at hub height (y=0) at t=5 s. Dark lines on V^* and W^* velocity contours represent an outline of U^* velocity from CFD data at B=4%.

distribution of W^* is relatively symmetric for the no-yaw case; however, for the yawed cases, the distribution was observed to be asymmetric with a larger magnitude of W^* along the direction of f_z . With downstream development, the W^* velocity component increases in the span-wise direction and is consistent with the deflection of the wake due to yaw.

The wake deflection and resultant asymmetry for a yawed inflow are three-dimensional in nature and, as a result, significantly

change the wake shape. This is best illustrated by observing planes that are perpendicular to the freestream. Wake velocity profiles and streamlines at a downstream location of x/D=4 are plotted in Fig. 8. The contour plots are normalized similar to Fig. 7; the physical extent of the wake, i.e., wake edge (99% of the free-stream, U_{99}), is shown in the velocity contour using a solid red line. For the no-yaw case, the wake is symmetric and has a nearly circular shape. The velocity deficit decreases radially outwards from the turbine's

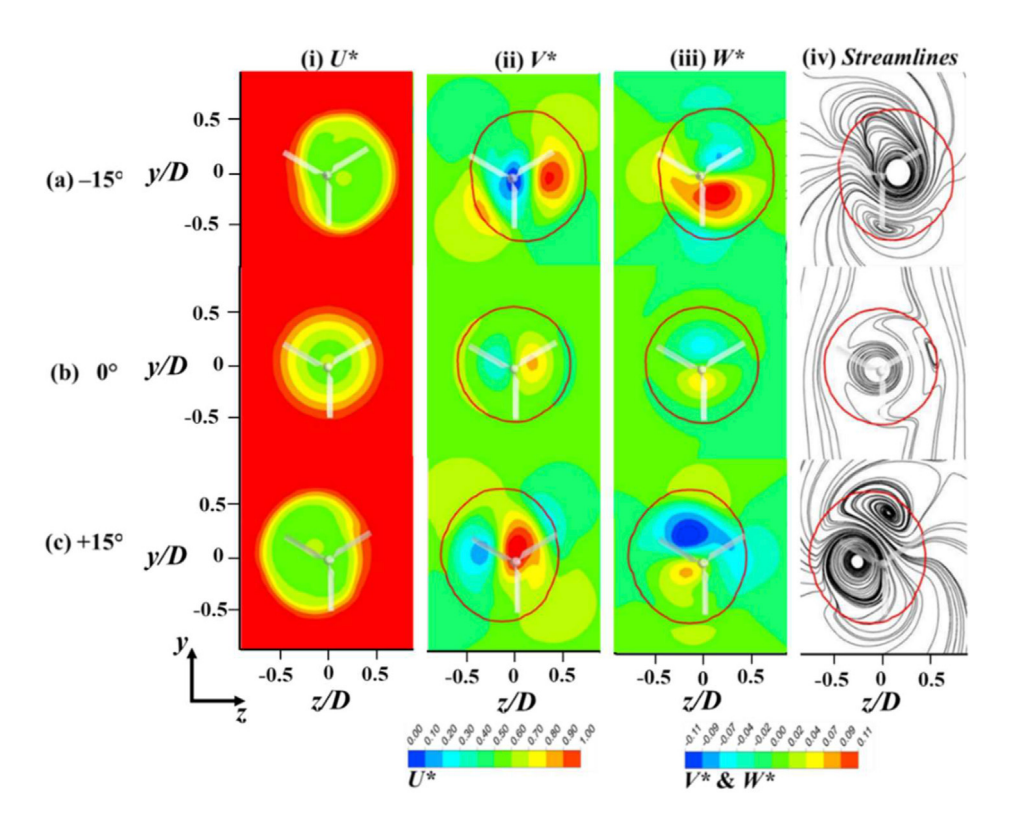


Fig. 8. Normalized velocities U^* , V^* , W^* , and streamlines for $\gamma=0^\circ$, -15° and $+15^\circ$ cases at a downstream location of x/D=4 at t=5 s. Dark lines on V^* and W^* velocity contour represents an outline of U_{99} . All plots based on CFD data at B=4%.

axis, and the cross-stream velocity components indicate a turbine wake rotating in a counter-clockwise direction. For the yawed cases, the distribution of wake velocity components was observed to be asymmetric, and the wake was observed to deflect in both vertical and cross-stream directions.

The presence of a strong and concentrated W* component inside the wake signifies the wake motion in the cross-stream direction that was observed either above or below the hub height depending on the direction of yaw, see Fig. 8c-(iii)-(iv). This flow feature is attributed to the counter-clockwise rotation of the turbine wake induced by the clockwise rotation of the TST. This crossstream momentum of the flow due to the turbine yaw leads to asymmetries in the downstream wake; a similar observation was made for a wake generated by a yawed wind turbine by Vollmer et al. [51]. In the absence of a rotating wake, as in the actuator disk experiments by Howland et al. [45], the strengthening of the crossstream velocity components was observed along the hub height as the wake did not have any associated induction effects. The observed wake compression along the cross-stream direction results in elongation in the vertical direction. This is better illustrated by the wake edge (red line) on the cross-stream contours [see Fig. 8 (ii) and (iii)] that show the wake moving upwards in the +y direction and in +z direction for -15° yaw case and in -z direction for $+15^{\circ}$ yaw case. The streamlines for both yawed and no-yaw cases [see Fig. 8(iv)] provide additional insights into the wake asymmetry. A single vortex is observed for the no-yaw case and is located at the wake center: the red line depicts the wake edge. For the vawed cases, two counter-rotating vorticity pair (CVP) is observed. As the CVP is transported downstream, the cross-stream velocity component (W^*) develops due to differences in vortex strength between the vortex pairs, resulting in varying wake displacement from the hub height (along y-direction). Similar observations were also reported in actuator-disk experiments by Howland et al. [45], where the CVP is symmetric, and rotating wake experiments [52,53], where asymmetry in the vortex pair was observed. CVP formation is not limited to turbines at yaw but also observed in jets that interact with a cross-flow [54].

3.2.2. Turbulence intensity

Fig. 9a—c plots the one-dimensional turbulence intensity (Ti) profiles at the three downstream locations using experimental data. A major portion of the turbulence generated in the wake is observed in the high shear regions around the tip of the blade and hub of the turbine for both yaw and no-yaw cases. For the no-yaw case, two distinct sets of peaks can be observed at the location close to the rotor, x/D = 0.5. The larger peaks are present in the wake edge between the wake and the bypass flow with a peak $Ti \sim 12-13\%$; the second set of smaller peaks occur closer to the wake center with Ti

~10% due to the shear layer formation by the interaction of the accelerated flow due to rope vortex and the slow-moving wake; similar to observations made by previous studies from our group [16]. As the wake propagates downstream to x/D = 2, the secondary set of peaks inside the wake can be observed to disappear, with peaks at the outer edge increase to a magnitude of $Ti = \sim 14-15\%$. For vawed wake, *Ti* profiles with one set of distinct peak at the outer edge of the wake can be observed with a magnitude slightly higher than the no-yaw case. However, unlike a no-yaw case, the magnitude of the peaks are different, suggesting asymmetricity in the wake. At x/D = 0.5, the magnitude of *Ti* near the wake edges varies between ~12%-16%. At this location, the inside of the wake for yawed case is highly turbulent compared to the no-yaw case. With increasing downstream distance, the Ti in the inner region of the wake was observed to decrease while the values near the edges increase to ~18% as it reaches x/D = 2. For yawed case, only a single peak is observed at x/D = 2, as the second half of the wake and corresponding shear layer could not be measured due to interference of flow between the nacelle and the test section.

3.3. Tracking the center of wake

Identifying wake trajectories in array configuration is important as it guides the downstream turbine units' positioning. The wake of the vawed rotor is deflected as it propagates downstream and is tracked with the help of the wake center. This aspect of a yawed wake is often used to steer the wake away from downstream turbine units and is referred to as yaw-based wake-steering. From a field experiment conducted by Howland et al. [31], such steering was observed to increase the cumulative energy extraction by the array by 47% in low-wind speed conditions and 13% at high wind speed conditions. The normalized center of wake coordinates was estimated using the center of mass technique based on planar twodimensional datasets, and the results are plotted in a 3D plot (see Fig. 10a). A simpler representation of the wake path is presented as a polar plot for all the inflow cases in Fig. 10b, where the numbers represent the downstream locations (x/D). For the no-yaw case, a negligible vertical meandering of the wake center occurs within a small bound of the turbine axis and is restricted to values < 0.04D. As expected, wake meandering is observed for both yaw angles. The wake's cross-stream meandering was noticeably larger, with a shift of ~0.2D in the center of the wake for up to a downstream distance of 5D. The magnitude of the vertical meandering of the wakecenter is less pronounced and was observed to be between ~0.05D - 0.12D about the hub height for locations x/D > 3. For the yawed cases at x/D < 2.5, vertical meandering for both the cases are negligible. Vertical meandering for the yawed cases is observed beyond $x/D \ge 3$. The direction of vertical meandering is dependent

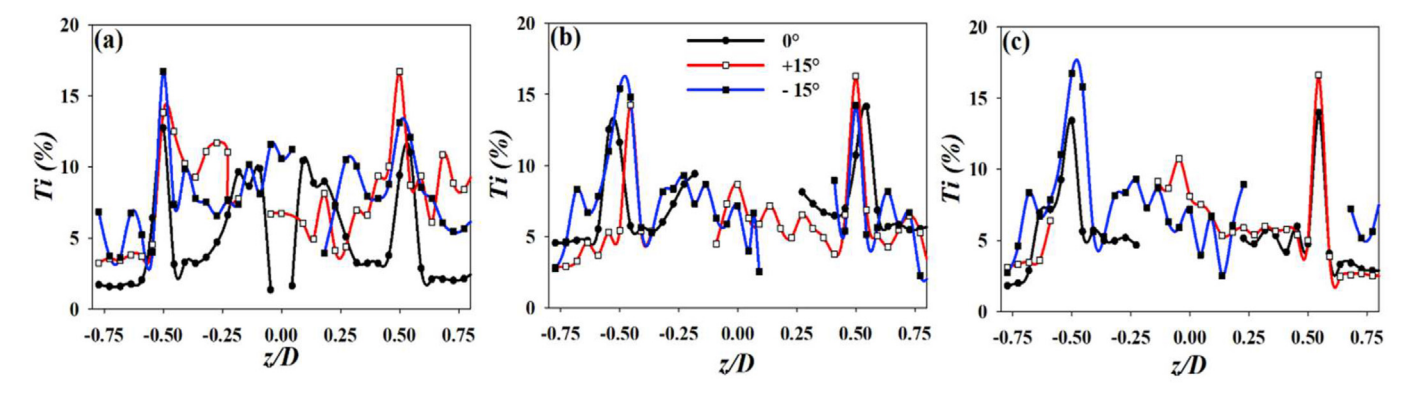


Fig. 9. Turbulence intensity profiles for $\gamma=0^{\circ}$, -15° and $+15^{\circ}$ at (a) x/D=0.5, (b) x/D=1, and (c) x/D=2 at hub height (y=0) from experimental data at B=16.5%.

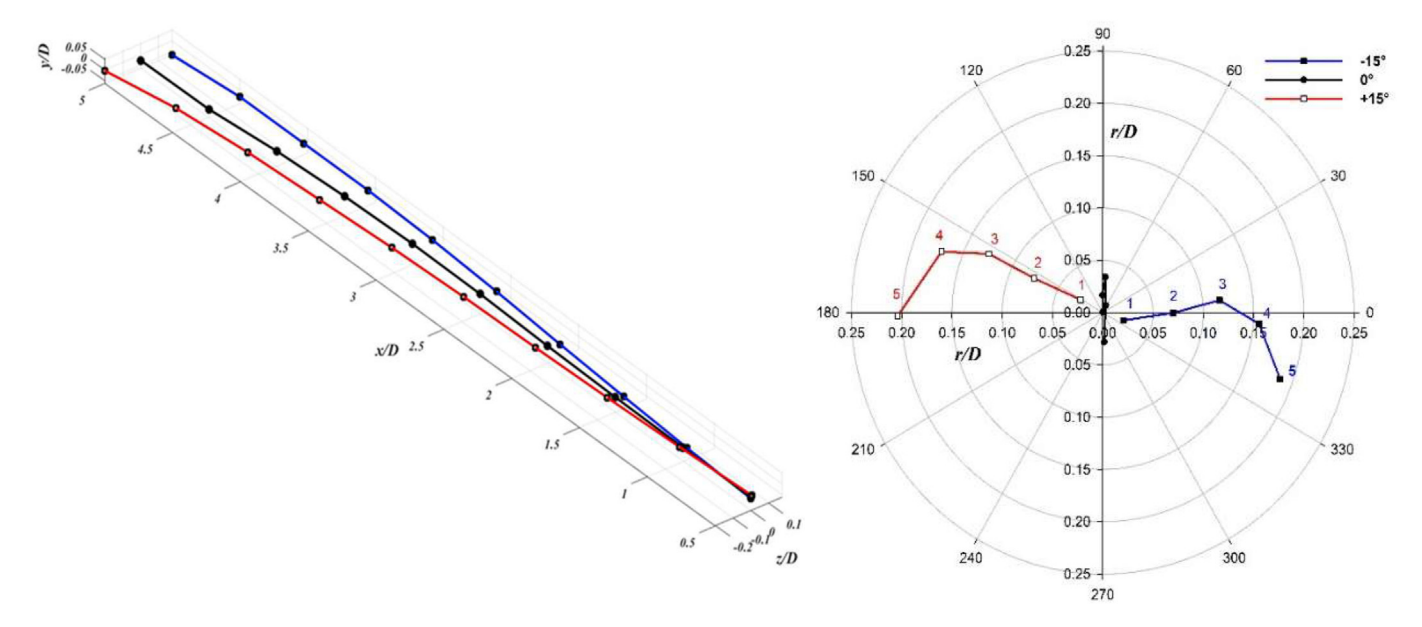


Fig. 10. Wake deflection trajectory using the two-dimensional technique at different downstream locations shown in (a) 3D plane and (b) Polar plane with the numbers representing non-dimensional downstream (x/D) locations. Plots based on CFD data at B=4%.

on the direction of yaw, with the wake moving towards the free surface for $+15^{\circ}$ yaw case and away from it for -15° yaw. The authors attribute this to be an artifact of wake rotation and deflection where the influx of cross-stream momentum into the deflected wake causes the wake deficit to accumulate in the lower half-plane (i.e., below hub-height of the rotor) for -15° yaw case or in the upper half-plane for the $+15^{\circ}$ yaw case. Consequently, the mean kinetic energy in the flow around the center of the wake takes the longest to recover. Thereby, in addition to wake-steering, estimating the wake center is also useful in determining downstream locations that should be avoided for placement considerations in an array [55,56]. The periodicity of the rotor wake and its interaction with the downstream turbine in an array determines optimum turbine array placement, and those aspects are discussed next.

3.4. Wake periodicities and their propagation

An array layout must be designed such that the downstream turbine(s) avoid direct interaction with periodic flow structures (like tip vortices) shed from upstream turbines in the array. The interaction of turbine components (especially turbine blades) with coherent structures causes higher load fluctuations on turbine blades leading to blade fatigue and a reduction in operational life, leading to operation and maintenance costs. The presence of such periodic structures can be discerned by performing a frequency analysis of the flow in the turbine wake [16]. Based on our measurements of Ti profiles across the wake (see Fig. 9), such discernible wake structures were observed at locations corresponding to peak Ti for both yaw and no-yaw experiments where tip vortices are present. Frequency spectra comparison at the location of maximum Ti (which occurs at wake edge) for the yaw and no-yaw cases at downstream locations of x/D = 0.5 and 2 are presented in Fig. 11. As seen in Fig. 11a, in the no-yaw case, spectral peaks can be identified at the rotational frequency of the rotor, F_R (4.1667 Hz), and its harmonics. At the closer downstream location of x/D = 0.5, the blade passing frequency F_B (= $3F_R$) is clearly the most dominant frequency component, suggesting the strong presence of blade tip vortices. As the wake propagates downstream, the spectral energy in the wake is observed to be redistributed, with F_R having the highest spectral energy and no identifiable harmonics beyond $2F_R$. This further suggests the presence of a coherently rotating wake with weaker/no tip vortices by x/D = 2. In the yawed wake, the spectral peaks observed at F_R and its harmonics were significantly weaker than in the no-yaw case. At x/D = 0.5, F_B was observed to have only ~40% of the amplitude (spectral energy) compared to the no-yaw case. At x/D = 2, $2F_R$ was the most dominant frequency component (again with considerably lesser energy), and a peak was identifiable even at $5F_R$. This observation further emphasizes the impact of increased interaction of the wake with the surrounding flow. The momentum flux into the wake resulting from yaw misalignment is seen to be capable of swiftly perturbing coherent flow structures in the wake that are more likely to dissipate away quicker with downstream evolution of the wake, further minimizing the risk of impingement on downstream turbine units.

3.5. Energy recovery due to turbine yaw

It is a common practice to utilize wake velocity profiles downstream of the turbine to estimate energy available/recovery in the wake [57]. In the current study, the energy available, *E*, at a particular downstream location of the turbine is estimated as [16]:

$$E = \frac{1}{2} \rho \sum_{i=1}^{N} A_i V_i^3 \tag{13}$$

where N is the number of area elements in the wake, A_i is the area, and V_i is the mean velocity in the element i. The total area considered at a given downstream plane is equivalent to the turbine rotor area; thus, this method ignores any wake expansion effects. Time-averaged velocity along the plane is extracted from the CFD simulations as a point cloud with a spacing of 0.0275D between the center of each element in both horizontal and vertical directions. Energy recovery at downstream locations was estimated as a fraction of the energy available in the free stream over an area equivalent to the turbine rotor $(\frac{1}{2}\rho AU_{\infty}^{3})$. The energy available to a turbine at a particular downstream location is also strongly dependent on its cross-stream position for the upstream turbine. A study by Draper et al. [58] compared staggered and inline layout for

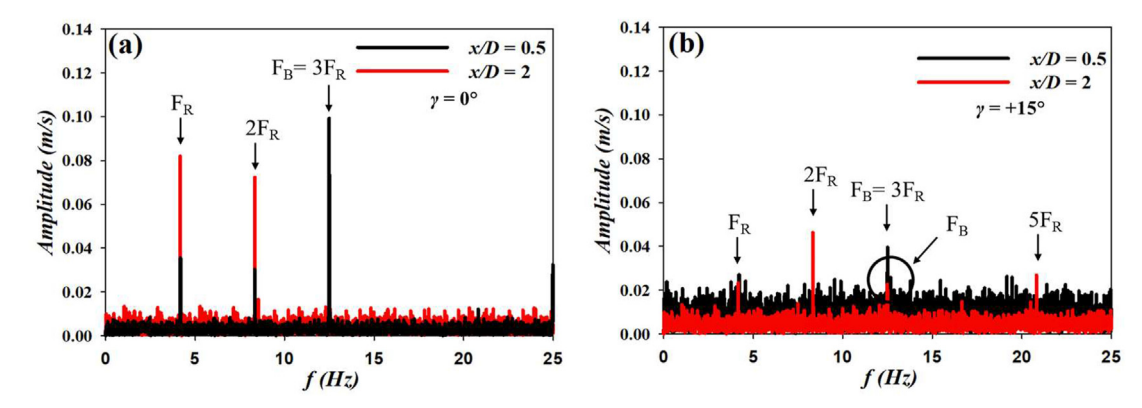


Fig. 11. Frequency spectrum of the streamwise velocity component at x/D = 0.5 and x/D = 2 for (a) $\gamma = 0^{\circ}$ and (b) $\gamma = +15^{\circ}$ at cross-stream location of peak TKE. Plots based on experimental data at B = 16.5%.

no-yawed turbine array where they observed the cumulative power output to maximize in staggered arrangement compared to the inline layout. They also observed that the spacing between turbine rows spacing for inline cases needs to be greater than in staggered cases.

In the current study, two similar approaches to downstream turbine placement are considered (see Fig. 12a). In the inline configuration, the downstream turbine is placed along the domain centerline, while in the staggered configuration, the downstream turbine is placed along the axis of the upstream turbine. Only an inline case is presented for the no-vaw configuration where the downstream turbines are located at the domain centerline, which coincides with the path of the propagating wake. Fig. 12b plots the energy recovery estimates for staggered and inline approaches for the yawed case and inline approach for the no-yaw case within the range 2 < x/D < 5. Since the recovery values were similar for $\pm 15^{\circ}$ yaw cases, only the $+15^{\circ}$ yaw case data is presented. From Fig. 12b, with the inline approach for downstream turbine placement, novaw case experiences maximized wake interaction resulting in minimal energy recovery of ~21%-32% as the wake propagates between 2 < x/D < 5 and wake steering due to the yawed upstream turbine resulted in an energy recovery between ~24 and 42%. The staggered approach (shown in Fig. 12a) resulted in significantly larger energy recovery between 64% and 100% for yawed case, as the wake was completely steered away from the turbine axis by a downstream distance of 4D. For the yawed turbine at inline placement, the wake partially interacts with the downstream turbine rotor even at x/D = 5, whereas the downstream rotor misses the wake completely in staggered placement when the upstream turbine is at yaw. For the yawed case, in addition to wake reenergization by cross-stream momentum transfer, the deflected nature of the wake also incites streamwise diffusion of momentum into the wake resulting in the enhanced rate of recovery. Similar observations were made in yawed wind turbines by Loland [53]; a faster wake recovery with an increase in vaw was reported primarily due to the increase in momentum transfer between the freestream and the deflected wake. In addition, a thinning of the wake around hub height was observed (see Fig. 8). The faster wake recovery due to cross-stream momentum transfer under yaw would allow for closely packed turbines in an array with the downstream turbine completely avoiding the wake of the yawed upstream turbine. Similar concepts of wake-steering have been demonstrated in wind arrays [26] and can also be utilized in a tidal array to reduce operations and maintenance costs, increase the annual energy production from the array, and a reduction in the Levelized cost of energy.

4. Conclusions

A synergistic experimental and transient CFD analysis was undertaken for a TST under yawed inflow conditions to analyze performance degradation, wake propagation, and energy recovery up

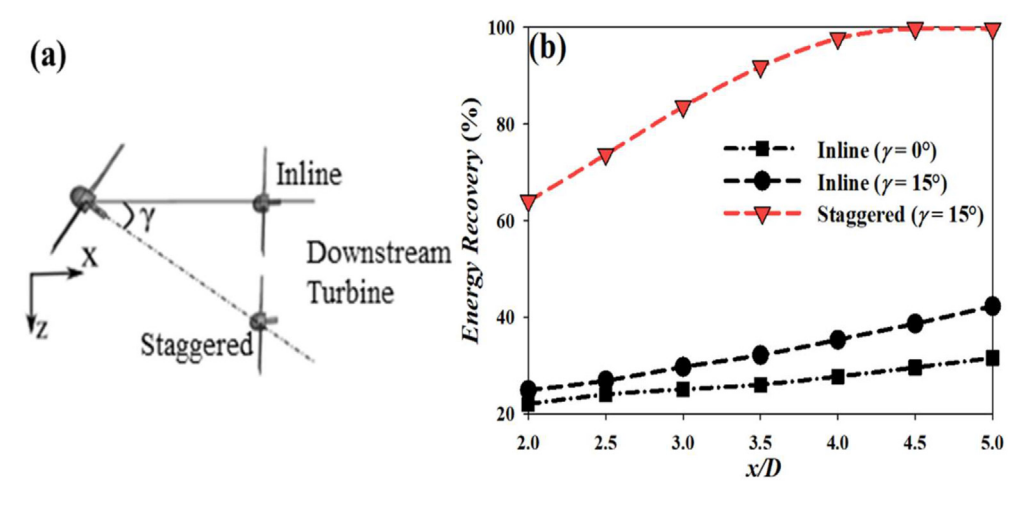


Fig. 12. (a) Schematic of the two different downstream turbine alignments with respect to the upstream turbine; (b) Energy recovery estimate for yaw case for different downstream turbine alignment cases. Plots based on CFD data at B = 4%.

P.K. Modali, A. Vinod and A. Banerjee Renewable Energy 177 (2021) 482–494

to a downstream distance of 5D from the rotor. A thorough understanding of near wake asymmetry and recovery was valuable in effectively implementing wake steering strategies to maximize TST power output in a tidal array. The main findings can be summarized as follows:

- In yawed inflows, turbine performance degradation of ~8.7% in C_P and ~9% in C_T was observed at $TSR \approx 4.8$, corresponding to C_P , max. A cosine fit with the power reduction index of 2.25 was observed to be the closest fit to relate reduction in power coefficient for yawed inflow.
- A yawed turbine wake was found to undergo considerable deflection away from the turbine axis and have an asymmetric cross-section due to the generation of a counter-rotating vortex pair (CVP) within the wake. The deflection also resulted in increased momentum flux into the wake resulting in quicker energy recovery.
- The increased momentum flux into the yawed wake was also found to abet the break-up of coherent flow structures in the wake, thereby minimizing the risk of impingement on downstream turbine units within a tidal array and consequent reduction in operations and maintenance costs.
- Energy recovery estimated downstream of the yawed rotor was higher compared to the no-yaw case. From the different turbine placement configurations explored, it was evident that the staggered approach that exploited the potential for wake steering was effective in reducing the required cross-stream and downstream spacing between turbine units in an array.

CRediT authorship contribution statement

Pranav K. Modali: Methodology, Software, Data curation, Investigation, Validation, Visualization, Formal analysis, Writing — original draft. **Ashwin Vinod:** Methodology, Data curation, Investigation, Visualization, Formal analysis, Writing — original draft. **Arindam Banerjee:** Methodology, Data curation, Investigation, Conceptualization, Investigation, Writing — review & editing, Supervision, Project administration, Funding acquisition.

Declaration of competing interest

The authors declare that they have no known competing financial interests or personal relationships that could have appeared to influence the work reported in this paper.

Acknowledgements

The authors acknowledge financial support from the U.S. National Science Foundation (CBET-Fluid Dynamics Program) through award # 1706358.

Appendix A. Supplementary data

Supplementary data to this article can be found online at https://doi.org/10.1016/j.renene.2021.05.152.

References

- M. Khan, G. Bhuyan, M. Iqbal, J. Quaicoe, Hydrokinetic energy conversion systems and assessment of horizontal and vertical axis turbines for river and tidal applications: a technology status review, Appl. Energy 86 (10) (2009) 1823—1835.
- [2] N. Kolekar, A. Banerjee, A coupled hydro-structural design optimization for hydrokinetic turbines, J. Renew. Sustain. Energy 5 (5) (2013), 053146.
- [3] T. Karthikeyan, E. Avital, N. Venkatesan, A. Samad, Design and analysis of a

marine current turbine, in: ASME 2017 Gas Turbine India Conference, American Society of Mechanical Engineers Digital Collection, 2017.

- [4] E.L.C. Arrieta, C. Cardona-Mancilla, J. Slayton, F. Romero, E. Torres, S. Agudelo, J.J. Arbelaez, D. Hincapié, Experimental investigations and CFD simulations of the blade section pitch angle effect on the performance of a horizontal-axis hydrokinetic turbine, Eng. J. 22 (5) (2018) 141–154.
- [5] S.S. Mukherji, N. Kolekar, A. Banerjee, R. Mishra, Numerical investigation and evaluation of optimum hydrodynamic performance of a horizontal axis hydrokinetic turbine. I. Renew. Sustain. Energy 3 (6) (2011), 063105.
- [6] N. Kolekar, S.S. Mukherji, A. Banerjee, Numerical modeling and optimization of hydrokinetic turbine, in: ASME 2011 5th International Conference on Energy Sustainability, 2011.
- [7] W. Batten, A. Bahaj, A. Molland, J. Chaplin, The prediction of the hydrodynamic performance of marine current turbines, Renew. Energy 33 (5) (2008) 1085–1096.
- [8] A. Bahaj, W. Batten, G. McCann, Experimental verifications of numerical predictions for the hydrodynamic performance of horizontal axis marine current turbines, Renew. Energy 32 (15) (2007) 2479–2490.
- [9] Z. Hu, X. Du, N.S. Kolekar, A. Banerjee, Robust design with imprecise random variables and its application in hydrokinetic turbine optimization, Eng. Optim. 46 (3) (2014) 393–419.
- [10] A. Mason-Jones, D. O'doherty, C. Morris, T. O'doherty, Influence of a velocity profile & support structure on tidal stream turbine performance, Renew. Energy 52 (2013) 23–30.
- [11] I. Rodriguez-Eguia, I. Errasti, U. Fernandez-Gamiz, J.M. Blanco, E. Zulueta, A. Saenz-Aguirre, A parametric Study of trailing edge flap Implementation on three different airfoils Through an artificial neuronal network, Symmetry 12 (5) (2020) 828.
- [12] N. Kolekar, S.S. Mukherji, A. Banerjee, Numerical modeling and optimization of hydrokinetic turbine, in: Energy Sustainability, 2011.
- [13] N. Kolekar, Z. Hu, A. Banerjee, X. Du, Hydrodynamic design and optimization of hydro-kinetic turbines using a robust design method, in: Proceedings of the 1st Marine Energy Technology Symposium METS13, 2013.
- [14] B. Dou, M. Guala, L. Lei, P. Zeng, Wake model for horizontal-axis wind and hydrokinetic turbines in yawed conditions, Appl. Energy 242 (2019) 1383–1395.
- [15] N. Kolekar, A. Banerjee, Performance characterization and placement of a marine hydrokinetic turbine in a tidal channel under boundary proximity and blockage effects, Appl. Energy 148 (2015) 121–133.
- [16] A. Vinod, A. Banerjee, Performance and near-wake characterization of a tidal current turbine in elevated levels of free stream turbulence, Appl. Energy 254 (2019), 113639.
- [17] M.Z. Zainol, N. Ismail, I. Zainol, A. Abu, W. Dahalan, A review on the status of tidal energy technology worldwide. Sci, Bar Int. 29 (2017) 659–667.
- [18] M. Nachtane, M. Tarfaoui, I. Goda, M. Rouway, A review on the technologies, design considerations and numerical models of tidal current turbines, Renew. Energy 157 (September) (2020) 1274–1288.
- [19] P. Bachant, M. Wosnik, Characterising the near-wake of a cross-flow turbine, J. Turbul. 16 (2015) 392–410.
- [20] M. Edmunds, A.J. Williams, I. Masters, A. Banerjee, J.H. VanZwieten, A spatially nonlinear generalised actuator disk model for the simulation of horizontal axis wind and tidal turbines, Energy 194 (2020), 116803.
- [21] P. Mycek, B. Gaurier, G. Germain, G. Pinon, E. Rivoalen, Experimental study of the turbulence intensity effects on marine current turbines behaviour. Part I: one single turbine, Renew. Energy 66 (2014) 729–746.
- [22] J. Thomson, B. Polagye, V. Durgesh, M.C. Richmond, Measurements of turbulence at two tidal energy sites in Puget Sound, WA, IEEE J. Ocean. Eng. 37 (3) (2012) 363–374.
- [23] T. Blackmore, L.E. Myers, A.S. Bahaj, Effects of turbulence on tidal turbines: implications to performance, blade loads, and condition monitoring, Int. J. Marine Energy 14 (2016) 1–26.
- [24] A. Vinod, C. Han, A. Banerjee, Tidal turbine performance and near-wake characteristics in a sheared turbulent inflow, Renew. Energy 175 (2021)
- [25] U. Ahmed, D. Apsley, I. Afgan, T. Stallard, P. Stansby, Fluctuating loads on a tidal turbine due to velocity shear and turbulence: comparison of CFD with field data, Renew. Energy 112 (2017) 235–246.
- [26] P. Galloway, Performance Quantification of Tidal Turbines Subjected to Dynamic Loading, University of Southampton, 2013.
- [27] P.K. Modali, N. Kolekar, A. Banerjee, Performance and wake characteristics of a tidal turbine under yaw, Int. J. Marine Energy (1) (2018) 1.
- [28] C.H. Frost, P.S. Evans, M.J. Harrold, A. Mason-Jones, T. O'Doherty, D.M. O'Doherty, The impact of axial flow misalignment on a tidal turbine, Renew. Energy 113 (2017) 1333–1344.
- [29] P.W. Galloway, L.E. Myers, A.S. Bahaj, Quantifying wave and yaw effects on a scale tidal stream turbine, Renew. Energy 63 (2014) 297–307.
- [30] M. Adaramola, P.-Å. Krogstad, Experimental investigation of wake effects on wind turbine performance, Renew. Energy 36 (8) (2011) 2078–2086.
- [31] M.F. Howland, S.K. Lele, J.O. Dabiri, Wind farm power optimization through wake steering, Proc. Natl. Acad. Sci. Unit. States Am. 116 (29) (2019) 14495—14500.
- [32] C. Frost, C.E. Morris, A. Mason-Jones, D.M. O'Doherty, T. O'Doherty, The effect of tidal flow directionality on tidal turbine performance characteristics, Renew. Energy 78 (2015) 609–620.
- [33] L. Chamorro, C. Hill, V. Neary, B. Gunawan, R. Arndt, F. Sotiropoulos, Effects of

- energetic coherent motions on the power and wake of an axial-flow turbine, Phys. Fluids 27 (5) (2015), 055104.
- [34] W. Tian, J.H. VanZwieten, P. Pyakurel, Y. Li, Influences of yaw angle and turbulence intensity on the performance of a 20 kW in-stream hydrokinetic turbine, Energy 111 (2016) 104–116.
- [35] S. Park, S. Park, S.H. Rhee, Influence of blade deformation and yawed inflow on performance of a horizontal axis tidal stream turbine, Renew. Energy 92 (2016) 321–332.
- [36] P.W. Galloway, L.E. Myers, A.S. Bahaj, Experimental and numerical results of rotor power and thrust of a tidal turbine operating at yaw and in waves, in: World Renewable Energy Congress-Sweden; 8-13 May, Linköping University Electronic Press, Linköping; Sweden, 2011, 2011.
- [37] F. Baratchi, T. Jeans, A. Gerber, Actuator line simulation of a tidal turbine in straight and vawed flows. Int. I. Marine Energy 19 (2017) 235–255.
- [38] F. Maganga, G. Germain, J. King, G. Pinon, E. Rivoalen, Experimental characterisation of flow effects on marine current turbine behaviour and on its wake properties, IET Renew. Power Gener. 4 (6) (2010) 498–509.
- [39] A. Bahaj, A. Molland, J. Chaplin, W. Batten, Power and thrust measurements of marine current turbines under various hydrodynamic flow conditions in a cavitation tunnel and a towing tank, Renew. Energy 32 (3) (2007) 407–426.
- [40] N. Kolekar, A. Vinod, A. Banerjee, On blockage effects for a tidal turbine in free surface proximity, Energies 12 (17) (2019) 3325.
- [41] K. Elliott, E. Savory, C. Zhang, R. Martinuzzi, W. Lin, Analysis of a curvature corrected turbulence model using a 90 degree curved geometry modelled after a centrifugal compressor impeller, in: 20th Annual Conference of the CFD Society of Canada. 2012.
- [42] F.R. Menter, M. Kuntz, R. Langtry, Ten years of industrial experience with the SST turbulence model, Turbulence, Heat Mass Transfer 4 1 (2003) 625–632, no.
- [43] P.E. Smirnov, F.R. Menter, Sensitization of the SST turbulence model to rotation and curvature by applying the Spalart–Shur correction term, J. Turbomach. 131 (4) (2009), 041010.
- [44] H. Ross, B. Polagye, An experimental evaluation of blockage effects on the wake of a cross-flow current turbine, J. Ocean Eng. Marine Energy 6 (3) (2020) 263–275
- [45] M.F. Howland, J. Bossuyt, L.A. Martínez-Tossas, J. Meyers, C. Meneveau, Wake structure in actuator disk models of wind turbines in yaw under uniform inflow conditions, J. Renew. Sustain. Energy 8 (4) (2016), 043301.
- [46] M. Shahsavarifard, E.L. Bibeau, Performance characteristics of shrouded

- horizontal axis hydrokinetic turbines in yawed conditions, Ocean. Eng. 197 (2020), 106916.
- [47] T.F. Pedersen, S. Gjerding, P. Enevoldsen, J. Hansen, H. Jørgensen, Wind turbine power performance verification in complex terrain and wind farms Risoe-R No. 1330(EN), Forskningscenter Risoe, Denmark, 2002.
- [48] X. Sun, J. Chick, İ. Bryden, Laboratory-scale simulation of energy extraction from tidal currents, Renew. Energy 33 (6) (2008) 1267–1274.
- [49] S. Rose, A. Good, M. Atcheson, G. Hamill, C. Johnstone, P. MacKinnon, D. Robinson, A. Grant, T. Whittaker, Investigating experimental techniques for measurement of the downstream near wake of a tidal turbine, in: Proceedings of the 9th European Wave and Tidal Energy Conference, 2011. Southampton, III
- [50] S. Rose, S.E. Ordonez Sanchez, C. Johnstone, T. Mccombes, A. Grant, K. Lee, C. Jo, Tidal turbine wakes: small scale experimental and initial computational modelling, in: 9th European Wave and Tidal Energy Conference, EWTEC 2011, 2011.
- [51] L. Vollmer, G. Steinfeld, D. Heinemann, M. Kühn, Estimating the wake deflection downstream of a wind turbine in different atmospheric stabilities&58; an LES study, Wind Energy Sci. 1 (2) (2016) 129–141.
- [52] J.M.S. Bartl, F.V. Mühle, J. Schottler, L.R. Sætran, J. Peinke, M.S. Adaramola, M. Holling, Wind tunnel experiments on wind turbine wakes in yaw: effects of inflow turbulence and shear, Wind Energy Sci. (2018). https://doi.org/10.5194/wes-3-329-2018.
- [53] H. Lee, D.-J. Lee, Wake impact on aerodynamic characteristics of horizontal axis wind turbine under yawed flow conditions, Renew. Energy 136 (2019) 383–397
- [54] K. Mahesh, The interaction of jets with crossflow, Annu. Rev. Fluid Mech. 45 (2013) 379–407.
- [55] J. Bartí, F. Mühle, J. Schottler, L. Sætran, J. Peinke, M. Adaramola, M. Hölling, Wind tunnel experiments on wind turbine wakes in yaw: effects of inflow turbulence and shear, Wind Energy Sci. 3 (1) (2018) 329–343.
- [56] J. Schottler, J. Bartl, F. Mühle, L. Sætran, J. Peinke, M. Hölling, Wind tunnel experiments on wind turbine wakes in yaw: redefining the wake width, Wind Energy Sci. 3 (1) (2018) 257–273.
- [57] M. Nuernberg, L. Tao, Experimental study of wake characteristics in tidal turbine arrays, Renew. Energy 127 (2018) 168–181.
- [58] S. Draper, T. Nishino, Centred and staggered arrangements of tidal turbines, J. Fluid Mech. 739 (2014) 72–93.